PERGAMON

International Journal of Heat and Mass Transfer 46 (2003) 695–704

International Journal of HEAT and MASS TRANSFER

www.elsevier.com/locate/ijhmt

Analytical and numerical studies on viscous energy dissipation in laterally driven microcomb structures

Ching-Shung Chen *, Chia-Fen Chou

Department of Aerospace Engineering, Tamkang University, Tamsui 251, Taiwan, ROC

Received 30 December 2001; received in revised form 31 July 2002

Abstract

Numerical and analytical studies on viscous air damping in laterally oscillating microcomb structures are discussed in this work. Previous investigators modeled this type of flow field using Couette and Stokes flow models. The numerical simulation results demonstrate that the flow is much more complex and quite different from the Couette or Stokes flow. The pumping and sucking motions at the edges of the oscillating electrode create a fluid brake. This fluid brake retards the horizontal movement of the flow and generates a strong vortex in the region between the oscillating electrode and the base material, which has not been reported before. The deceleration of the fluid also increases the velocity gradient on the surfaces of the oscillating electrode, which gives rise to a higher damping. The numerically predicted damping is about 2.8 times larger than that predicted by the Stokes flow model.

Keywords: Accelerometer; Microcomb structure; Viscous damping

1. Introduction

On going advances in semiconductor fabrication technology have led to a new generation of sensors and actuators. Among these new devices are the laterally driven microactuators and microsensors. In contrast to vertically driven devices, with damping provided by the fluid squeeze-film produced by the relative axial or tilting motion of two closely spaced plates [1], the viscous shear in thin fluid films is the dominant damping mechanism in laterally moving microstructures. The attractive features of laterally driven microstructures have been proven by resonant sensors and actuators [2,3], frequency selective microfilters and damped microaccelerometers [4]. The damping level of a microstructure plays an important role in the performance of a system. For example, adequate damping is needed to obtain flat output signals over wide frequency ranges and prevent amplitude and phase distortions [4].

Fig. 1 shows a typical laterally moving microcomb structure, consisting of a mass suspended with tethers anchored onto the sensor body. For convenience and to avoid confusion we will refer this as a type I microstructure. Each pair of fixed and moving electrodes constitutes a differential capacitor. The lateral motion of the moving mass alters the distance between the capacitor and changes the output voltage. The output voltage of the system is nearly linear if the lateral motion amplitude of the moving mass is small. In order to maintain system sensitivity, the stiffness of the supporting tethers should be kept small.

The characteristic feature of the type I microcomb structure, Fig. 1, is that its oscillating direction is perpendicular to the longitudinal axis of the moving electrode and its oscillating amplitude is small. Because the output voltage of each capacitor is small, a series of capacitors are usually combined together to produce higher output voltage. Typical examples of such microstructures are ADXL-05 and -50 developed by the Analog Device Corporation and utilized in airbag systems. Studies on the dynamic behavior of type I microcomb structures are scarce in the literature. Another type of resonant microstructure, which we will refer to as type

* Corresponding author. Tel.: +1-886-2-2621-5656x2577; fax: +1-886-2-2620-9746.

E-mail address: cschen@mail.tku.edu.tw (C.-S. Chen).

0017-9310/03/$ - see front matter
PII: S0017-9310(02)00337-X

Nomenclature

d	distance between oscillating electrodes and base material (m)
d_c	gap between oscillating and fixed electrodes (m)
D	dissipation energy (J)
e	factor = 2.71828
E	strain energy of the comb structure (J)
h	height of oscillating electrodes (m)
l	length of oscillating electrodes (m)
K	equivalent stiffness of the supporting tethers for the seismic mass (N/m)
Kn	Knudsen number $= \lambda/d$
L	characteristic length = one half width of the computational domain (m)
M	mass of the movable comb structure (kg)
p	dimensional pressure (N/m^2)
$\overline{P}$	non-dimensional pressure
Q	quality factor $= 2\pi E/D$
Re	Reynolds number $= \rho v_0 L/\mu$
St	Strouhal number $= L\omega/v_0$
V	dimensional velocity in Y-direction (m/s)
$\overline{V}$	non-dimensional velocity in $\overline{Y}$-direction
v_0	lateral velocity of the oscillating electrode (m/s)
$\overline{W}$	non-dimensional velocity in $\overline{Z}$-direction
W_c	width of oscillating electrodes (m)
Y	dimensional Y-coordinate (m)
$\overline{Y}$	non-dimensional Y-coordinate
Z	dimensional Z-coordinate (m)
$\overline{Z}$	non-dimensional Z-coordinate

Greek letters

β_n	convenient parameter $= Ln\pi/d$
τ	non-dimensional time $= \omega t$
χ_w	shear stress at wall (N/m^2)
ρ	air density (kg/m^3)
ω	resonant frequency of the oscillating electrode (rad/s)
δ	penetration depth (m)
γ	non-dimensional parameter $= St\,Re$
λ	mean free path of air molecules (m)
σ	ratio of diffusively reflected molecules
ς	damping ratio $= 1/2Q$

Subscripts

I, II, III, IV	section I–IV
n	nth term in a series
w	wall

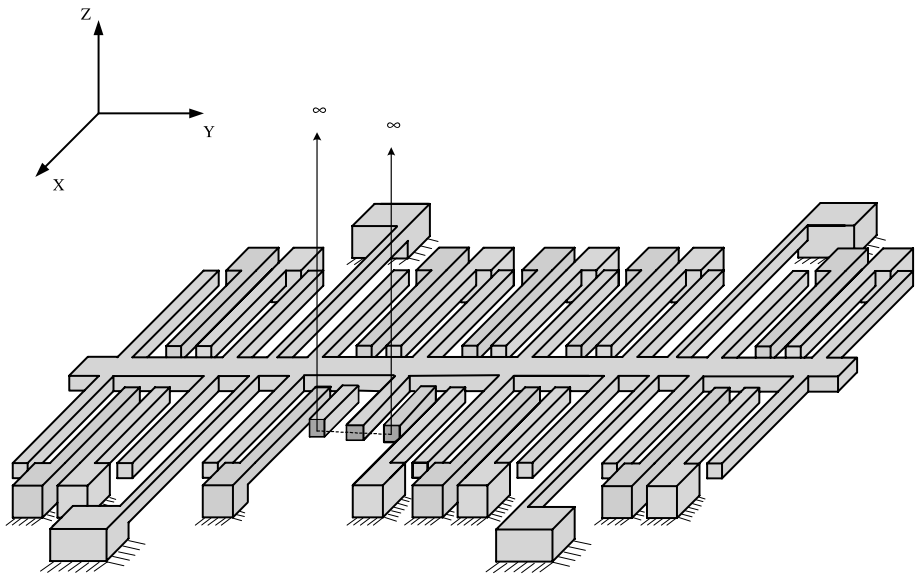

Fig. 1. The schematic diagram of a type I microcomb structure.

II, oscillating in the direction parallel to the longitudinal axis of the oscillating electrode is shown in Fig. 2. The dynamic performance of type II microstructures was studied by several investigators experimentally as well as analytically [3–5]. Type II microstructures have a larger oscillating amplitude. The purpose of this study is to

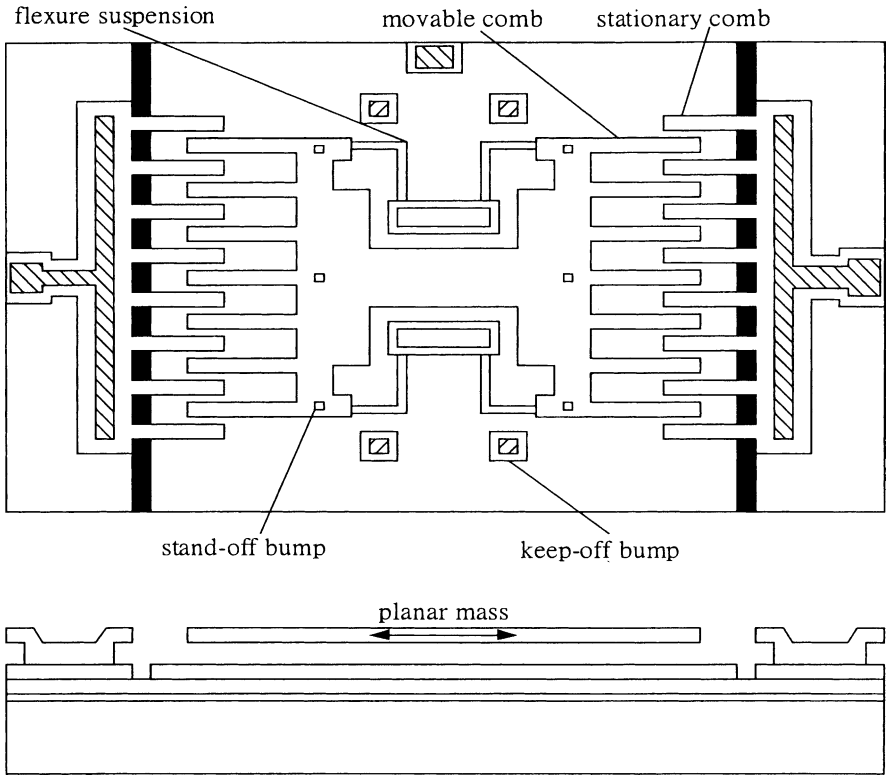

Fig. 2. The schematic diagram of a type II microcomb structure.

develop numerical schemes that are able to simulate the flow field of type I microcomb structures.

Because studies on the dynamic performance of type I microcomb structures are scarce in the literature, we introduce research work conducted on the dynamic performance of type II microcomb structures. Tang et al. [3] investigated viscous air damping in type II microcomb structures based on a Couette flow model. The theoretically estimated quality factors, Q, although qualitatively consistent with the measured Q, were much higher than the measured values. Cho et al. [4] studied this problem (type II) by modeling the flow between the oscillating electrode and the base material as a Stokes-type flow. The quality factors calculated by the Stokes-type flow model were in better agreement with the experimental data than factors computed using the Couette-type flow model. However, large discrepancies still remained between the estimated and measured Q. Zhang and Tang [5] developed an empirical formula based on experimental data to include the edge and finite-size effects (type II). This formula was based on a very limited database and has not been extensively validated.

The Couette and Stokes flow models are the only available analytical investigations seen in the literature besides experimental work. Knudsen numbers in typical microcomb structures indicate that part of the flow is in the slip flow region. The influence of the slip effect on viscous damping has not been reported. This study investigates this problem analytically as well as numerically. The slip effect is also included in this study.

2. Analytical solutions

2.1. Governing equations

Because the gaps in a microcomb structure are usually quite small compared to its length (Fig. 1), the flow in a cross-section parallel to its oscillating direction can be assumed to be two-dimensional. The governing equations are the unsteady two-dimensional incompressible Navier–Stokes equations, which are expressed in non-dimensional form in the following:

$$\frac{\partial \overline{V}}{\partial \overline{Y}} + \frac{\partial \overline{W}}{\partial \overline{Z}} = 0 \tag{1}$$

$$St\,Re\frac{\partial \overline{V}}{\partial \tau} + Re\left(\overline{V}\frac{\partial \overline{V}}{\partial \overline{Y}} + \overline{W}\frac{\partial \overline{V}}{\partial \overline{Z}}\right) = -\frac{\partial \overline{P}}{\partial \overline{Y}} + \left(\frac{\partial^2 \overline{V}}{\partial \overline{Y}^2} + \frac{\partial^2 \overline{V}}{\partial \overline{Z}^2}\right) \tag{2}$$

$$St\,Re\frac{\partial \overline{W}}{\partial \tau}+Re\left(\overline{V}\frac{\partial \overline{W}}{\partial \overline{Y}}+\overline{W}\frac{\partial \overline{W}}{\partial \overline{Z}}\right)=-\frac{\partial \overline{P}}{\partial \overline{Z}}+\left(\frac{\partial^2 \overline{W}}{\partial \overline{Y}^2}+\frac{\partial^2 \overline{W}}{\partial \overline{Z}^2}\right) \tag{3}$$

The physical quantities are normalized using the following relations:

$$\overline{Y}=Y/L,\quad \overline{Z}=Z/L,\quad \overline{V}=V/v_0,\quad \overline{W}=W/v_0,$$
$$\overline{P}=(P-P_\infty)/(\mu v_0/L),\quad \tau=\omega t$$

The parameter Re and St are the Reynolds and Strouhal numbers, respectively, and are defined by $Re=\rho v_0 L/\mu$, $St=L\omega/v_0$.

2.2. The solution of region I

In deriving the analytical solutions (Fig. 3), the oscillating electrode was assumed to be infinite, making this problem a flow over an impulsively started oscillating plate. The $\overline{W}$ velocity vanishes. The governing equation and the corresponding boundary conditions are

$$\gamma\frac{\partial \overline{V}_0}{\partial \tau}=\frac{\partial^2 \overline{V}_0}{\partial \overline{Z}^2} \tag{4}$$

$$\overline{V}_0=\cos\tau\quad \text{for } \overline{Z}=\frac{d+h}{L}$$
(on the oscillating electrode) (5)

$$\overline{V}_0=0\quad \text{for } \overline{Z}\to\infty$$
(far away from the oscillating electrode) (6)

where $\gamma=St\,Re$. Eq. (4) is a parabolic equation that can be solved using the separation of variables method [6]. The result is

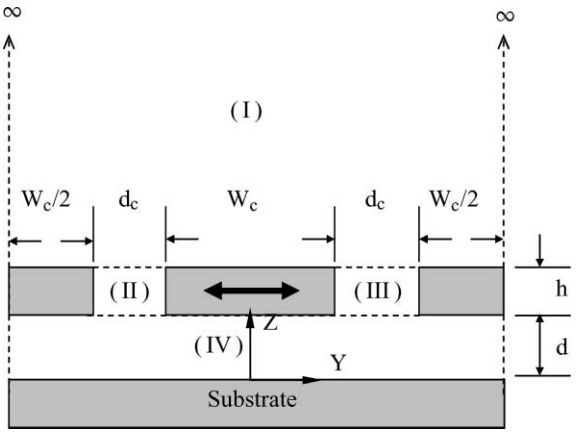

Fig. 3. The coordinate system for the analytical and numerical solutions.

$$\overline{V}_0(\tau,\overline{Z})=-\frac{2}{\sqrt{\pi}}\int_0^{\frac{1}{2}\sqrt{\frac{\gamma}{\tau}}\left(\overline{Z}-\frac{d+h}{L}\right)}\cos\left(\tau-\frac{\gamma}{4\mu^2}\left(\overline{Z}-\frac{d+h}{L}\right)\right)\times\exp(-\mu^2)\,\mathrm{d}\mu+\exp\left(-\sqrt{\frac{\gamma}{2}}\left(\overline{Z}-\frac{d+h}{L}\right)\right)\times\cos\left(\tau-\sqrt{\frac{\gamma}{2}}\left(\overline{Z}-\frac{d+h}{L}\right)\right) \tag{7}$$

The first term in the above equation represents the transient motion, which dies down after some time. The second term denotes the steady state motion of a type I microcomb structure. The energy dissipated by the viscous shear per oscillating cycle in region I can be calculated using

$$D_{\mathrm{I}}=\int_{A_1}\int_0^{2\pi/\omega}\chi_{\mathrm{w}}v_0\cos\omega t\,\mathrm{d}t\,\mathrm{d}A \tag{8}$$

The parameter χ_{w} is the viscous shear at the wall and $v_0\cos\omega t$ is the velocity of the oscillating electrode.

2.3. The solution of region IV

The governing equation and the corresponding boundary conditions are

$$\gamma\frac{\partial \overline{V}_0}{\partial \tau}=\frac{\partial^2 \overline{V}_0}{\partial \overline{Z}^2} \tag{9}$$

$$\overline{V}_0=0\quad \text{for } \overline{Z}=0\quad \text{(on the silicon substrate)} \tag{10}$$

$$\overline{V}_0=\cos\tau\quad \text{for } \overline{Z}=d/L$$
(on the oscillating electrode) (11)

Eq. (9) is a parabolic equation that can be solved using the separation of variables method [7,8]. The result is

$$\overline{V}_0(\tau,\overline{Z})=\frac{2L}{d}\sum_{n=1}^{\infty}\frac{(-1)^n\beta_n^3}{\beta_n^4+\gamma^2}\sin(\beta_n\overline{Z})\exp(-\beta_n^2\tau/\gamma)+\frac{L}{d}\overline{Z}\cos\tau+\frac{2L}{d}\sum_{n=1}^{\infty}\frac{(-1)^n\beta_n\gamma}{\beta_n^4+\gamma^2}\times\sin(\beta_n\overline{Z})\left(\frac{\gamma}{\beta_n^2}\cos\tau+\sin\tau\right) \tag{12}$$

The first term in the above equation represents the transient motion, which dies down after some time. The second and third terms denote the steady state motion of a type I microcomb structure. The energy dissipated by the viscous shear per oscillating cycle in region IV can be calculated using Eq. (8).

The strain energy of a microcomb structure is

$$E=\frac{1}{2\omega}v_0^2\sqrt{MK} \tag{13}$$

where M is the seismic mass of a microcomb structure and K denotes the equivalent stiffness of the supporting tethers for the seismic mass. The strain energy of a microcomb structure is dissipated by the viscous shear (region I and IV) and squeezing work (region II and III). The quality factor, Q, is defined as

$$Q = 2\pi\frac{E}{D} \tag{14}$$

where $D = D_{\mathrm{I}} + D_{\mathrm{II,III}} + D_{\mathrm{IV}}$. The damping ratio of a microcomb structure is defined by

$$\varsigma = \frac{1}{2Q} \tag{15}$$

3. Numerical solutions

3.1. The numerical boundary conditions

Because the oscillating amplitude is small compared with the width of the oscillating electrode (Fig. 3) the movement of the electrode was approximated using fluid injection and suction on the edges of the oscillating electrode. In the numerical simulations the oscillating electrode was fixed, but a $\cos\tau$ velocity was imposed on the upper and lower surfaces as well as on both edges of the oscillating electrode. The non-dimensional boundary conditions are

(1) $\overline{V} = \overline{W} = 0$, on the surfaces of fixed electrodes.
(2) $\overline{V} = \cos\tau$, $\overline{W} = 0$, on the surfaces of oscillating electrodes.
(3) $\overline{V} = \overline{W} = 0$, on the silicon substrate ($\overline{Z} = 0$).
(4) $\dfrac{\partial\overline{V}}{\partial\overline{Z}} = \dfrac{\partial\overline{W}}{\partial\overline{Z}} = \dfrac{\partial\overline{P}}{\partial\overline{Z}} = 0$, as $\overline{Z} \to \infty$.
(5) Periodic boundary conditions were utilized on the left and right boundaries.
(6) The slip boundary conditions were used if the slip flow assumption was assumed.

These boundary conditions were derived as follows:

The mean free path, λ , of the air under standard atmospheric conditions is about 0.06 μm. The gap, d, in regions II, III, and IV for a typical microcomb structure is about 2 μm. The Knudsen number in these regions is $Kn = \lambda/d = 0.03$, which indicates that the flow is in the slip flow region and the slip effects must be taken into account. For slip flows the fluid can be assumed to be a continuum but the slip boundary conditions must be utilized to account for the incomplete momentum exchange between the gas molecules and the walls.

Assuming an infinite plate is oscillating with a velocity $v_0\cos\omega t$ and the flow above it is a slip flow. Adjacent to the plate are gas molecules, one half of which were reflected from the plate, the other half originate from, on the average, a mean free path away from the plate. The velocity of the gas molecules a mean free path away from the plate can be expressed as a Taylor's expansion [9]

$$V_{Z=\lambda} = V_{Z=0} + \lambda\left(\frac{\partial V}{\partial Z}\right)_{Z=0} \tag{16}$$

The molecules reflected diffusively from the plate will have the tangential velocity of the plate. The molecules reflected specularly from the plate will have the same tangential velocity as those from a mean free path away from the plate. We assumed that σ is the ratio of diffusively reflected molecules. The tangential velocity of gas molecules adjacent to the plate is the average of the velocity of the incoming molecules and the velocity of the reflected molecules.

$$\begin{aligned} V_{Z=0} &= \frac{1}{2}\left[V_{Z=0} + \lambda\left(\frac{\partial V}{\partial Z}\right)_{Z=0}\right] \\ &\quad + \frac{1}{2}\left[(1-\sigma)\left(V_{Z=0} + \lambda\left(\frac{\partial V}{\partial Z}\right)_{Z=0}\right) + \sigma v_0\cos(\omega t)\right] \\ &= \frac{2-\sigma}{\sigma}\lambda\left(\frac{\partial V}{\partial Z}\right)_{Z=0} + v_0\cos(\omega t) \end{aligned} \tag{17}$$

If the plate is fixed then the slip boundary condition becomes

$$V_{Z=0} = \frac{2-\sigma}{\sigma}\lambda\left(\frac{\partial V}{\partial Z}\right)_{Z=0} \tag{18}$$

In general, the coefficients σ may depend on the surface's roughness, temperature, and the gas type. We assumed that $\sigma = 1$ in this study. The slip W velocity in regions II and III can also be derived in a similar way.

The slip boundary conditions were used on the side surfaces of the electrodes, i.e. the surfaces of regions II and III, and the top and bottom surfaces in region IV, if the slip flow assumption was specified.

3.2. The numerical procedure

The governing equations for the numerical simulations were Eqs. (1)–(3). To avoid pressure oscillations the Marker and Cell finite difference scheme in conjunction with a stagger grid was utilized [10]. An explicit finite difference scheme was used to discretize the governing equations. The computer program was validated first using the cavity flow problem, it was found that for very small Reynolds number flows an implicit scheme could only use a Δt twice large as that for an explicit scheme due to the stability constraint. However, the programming for the implicit scheme was much more complicated than that for the explicit scheme. We decided to adopt the explicit scheme for ease of programming. The convection and diffusion terms in the governing equations were central differenced. The nonlinear terms in the finite difference equations were

linearized by lagging the coefficients. The truncation error was therefore $O(\Delta\tau) + O(\Delta\overline{Y})^2 + O(\Delta\overline{Z})^2$.

The momentum equations, Eqs. (2) and (3), were differentiated with respect to $\overline{Y}$ and $\overline{Z}$, respectively, and added together to obtain a Poisson equation for pressure.

$$\frac{\partial^2\overline{P}}{\partial\overline{Y}^2}+\frac{\partial^2\overline{P}}{\partial\overline{Z}^2}=-StRe\frac{\partial\overline{S}}{\partial\tau}-Re\frac{\partial^2\overline{V}^2}{\partial\overline{Y}^2}-2Re\frac{\partial\overline{V}\overline{W}}{\partial\overline{Y}\partial\overline{Z}}-Re\frac{\partial^2\overline{W}}{\partial\overline{Z}^2}+\frac{\partial^2\overline{S}}{\partial\overline{Y}^2}+\frac{\partial^2\overline{S}}{\partial\overline{Z}^2} \tag{19}$$

where $\overline{S}=\frac{\partial\overline{V}}{\partial\overline{Y}}+\frac{\partial\overline{W}}{\partial\overline{Z}}$. The expression $\overline{S}^{n+1}=\left(\frac{\partial\overline{V}}{\partial\overline{Y}}+\frac{\partial\overline{W}}{\partial\overline{Z}}\right)^{n+1}$ in the $\partial\overline{S}/\partial\tau$ term was set equal to zero, because when the pressure field converges at the $n+1$ time step the continuity equation should be satisfied [10].

In the numerical simulations, the Poisson equation was solved first by iteration to obtain the pressure. The convergence criterion for the pressure field was $\sum|\overline{P}_{i,j}^{k+1}-\overline{P}_{i,j}^{k}|\leqslant 10^{-4}$, the superscription k is the iteration number. After convergence, the pressure was then substituted into the momentum equations, Eqs. (2) and (3), to solve for the $\overline{V}$ and $\overline{W}$ velocities. This completed one time step. This process continued until the periodic steady state was reached. The convergence criterion for the periodic steady state was

$$\sum\left|\overline{V}_{i,j}^{n+1}-\overline{V}_{i,j}^{n}\right|\leqslant 10^{-4} \tag{20}$$

where n is the oscillating cycles of the electrode. Eq. (20) was applied at the beginning of each oscillating cycle, if the criterion was met the calculation stopped. This process was time accurate.

3.3. Grid independence test and the grid

The value of $ReSt$ and Re for the model microstructure (Table 1) are 0.12 and 0.00083, respectively. The stability constraint was dominated by the parameter $ReSt$. Due to the small $ReSt$ value, a very small time step, $\Delta\tau=5\times10^{-6}$, was required in the numerical simulations. This study adopted a uniform grid. The computational domain for this study consists of 62 grids in the $\overline{Y}$-axis and 52 grids in the $\overline{Z}$-axis. It took about 48 h CPU time in a Pentium IV 1.5G PC to run an electrode oscillating cycle. Four oscillating cycles were required to satisfy the periodic steady state criterion described by Eq. (20). The boundary in the $\overline{Z}$ direction extends from $\overline{Z}=0$ to $5d$ with d the gap in region IV.

Table 1
Dimensions and parametric values of the type I microcomb structure [11]

Structure thickness (h)	1.8 μm
Air film thickness (d)	2.0 μm
Finger width (W_c)	4.0 μm
Finger gap (d_c)	2.0 μm
Effective damping area in region II and III	0.54×10^4 μm^2
Effective damping area in region I or II	2.93×10^4 μm^2
Equivalent stiffness (K)	3.08×10^{-7} N/μm
Effective mass (M)	0.123 μg
Resonant frequency	7.98 kHz
Reynolds number (Re)	0.00083
Strouhal number (St)	144.58

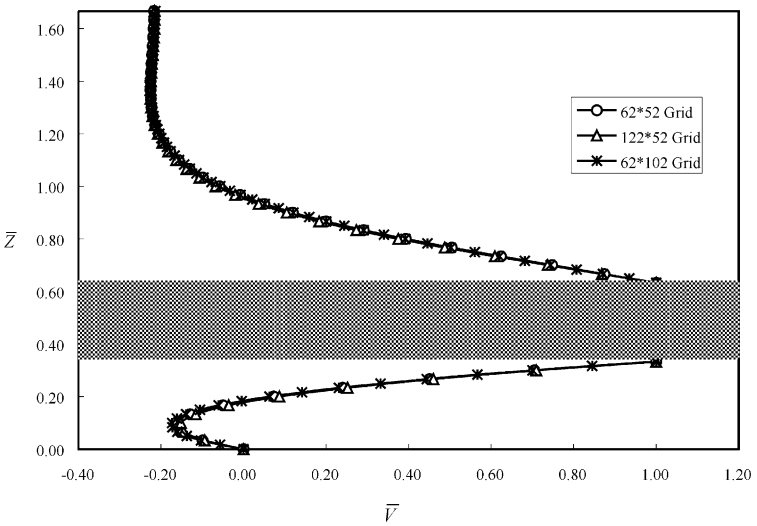

Fig. 4. The $\overline{V}$ velocity comparison along the $\overline{Y}=0$ axis for the 62×52 grid, 122×52 grid, and 62×102 grid, $ReSt=12$.

Because it was very time consuming to run $ReSt = 0.12$ cases, we decided to conduct a grid independence test on $ReSt = 12$ cases. A 62×52 grid, a 122×52 grid, and a 62×102 grid were simulated with $ReSt = 12$. The $\overline{V}$ velocity distributions along the $\overline{Y} = 0$ axis for the three grids are depicted in Fig. 4. The difference is very small as shown in Fig. 4. The 62×52 grid was chosen for the $ReSt = 0.12$ simulation cases.

In order to study the influence of the boundary extent in the $\overline{Z}$ direction on the results, a case with $ReSt = 12$, a 62×102 grid, and the vertical boundary extending to $10d$ was simulated. The results show that extending the boundary does not affect damping in region IV, but damping in region I increases 2.5%. The distance of the top boundary to the oscillating electrode does have a small effect on the results. In the $ReSt = 0.12$ simulation cases the vertical boundary was extended to $5d$ due to computing time considerations.

4. Results and discussion

In order to validate the numerical solutions, the numerical procedure was used to calculate the flow field of a type I microcomb structure. The dimensions and required parameters of this model are listed in Table 1 [11]. Fig. 5 depicts the streamline plot at $\tau = 0$ after the periodic steady state is reached. It took four oscillating cycles for the calculation to reach the periodic steady state. The convergence criterion was described by Eq. (20). The boundary conditions are the nonslip conditions. The flow field in region IV is quite different from the Stokes flow. The oscillating electrode moves to the right at its maximum velocity at $\tau = 0$. Its right edge pushes the fluid out of region III and forces the fluid to go upward and downward. The downward moving fluid in region IV behaves like a fluid brake, which retards the right moving fluid in region IV and forces it to turn back to form a vortex. The left edge of the oscillating electrode sucks the fluid into region II. The upward moving fluid at the intersection of region II and IV also acts like a fluid brake, which forces the left moving fluid near the substrate of region IV to turn back and helps to form the vortex in region IV. The flow in region IV is a vortex and cannot be modeled by the Stokes flow model.

The penetration depth in a Stokes flow, defined as a distance over which the surface motion amplitude decreases by a factor of e, is much greater than the gap d in region IV. The penetration depth calculated by the Stokes flow model is $\delta = \sqrt{2\nu/\omega}$ [12], which gives a numerical value of 24.5 μm for the present model (Table 1). This indicates that the penetration depth is far greater than the gap d, 2 μm, in region IV. The flow field can very quickly detect any changes in the boundary conditions. The vortex flow in region IV is influenced strongly by the boundary conditions but very weakly by the parameters Re and $ReSt$. The numerical simulations proved this. We changed $ReSt$ from 0.12 to 12. The vortex in region IV was nearly identical for the two cases.

The flow in region I is also different from the Stokes flow. The pumping and sucking motions of the oscillating electrode are significant as shown in Fig. 5. The upward moving fluid from region III again acts like a fluid brake and slows down the velocity of the right moving fluid in region I. Fig. 6 depicts the streamline plot at $\tau = \pi/2$ after the periodic steady state is reached.

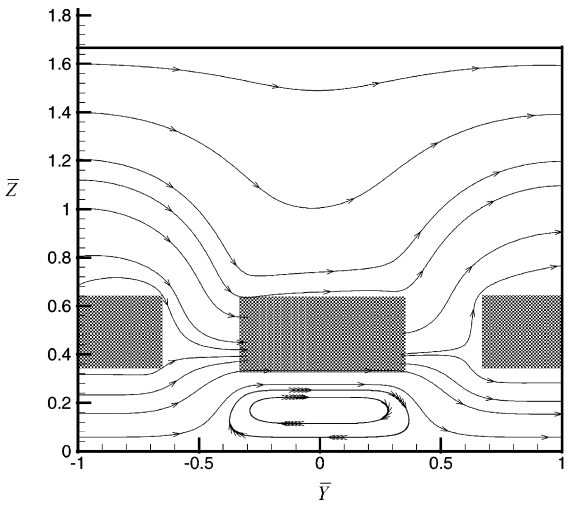

Fig. 5. The streamline plot at $\tau = 0$ subject to the nonslip boundary conditions after the periodic steady state is reached.

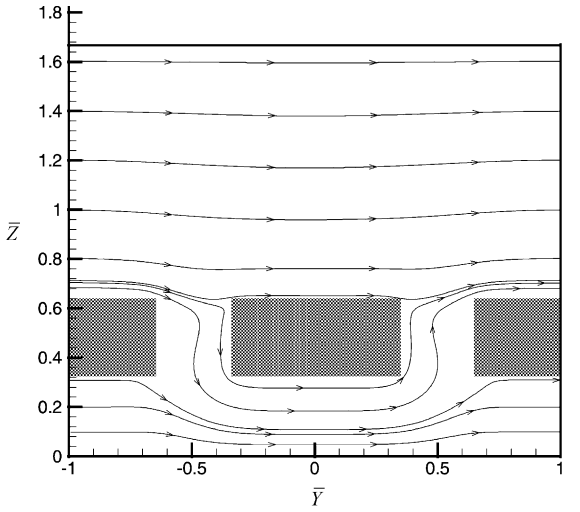

Fig. 6. The streamline plot at $\tau = \pi/2$ subject to the nonslip boundary conditions after the periodic steady state is reached.

The boundary conditions are the nonslip conditions. At this instant the oscillating electrode reaches its right most position and its velocity is zero. The fluid still moves but the velocity is nearly zero everywhere in the flow field and this is consistent with the physical phenomenon. Fig. 7 shows the streamline plot at $\tau = \pi$ after the periodic steady state is reached and the boundary conditions are the nonslip conditions. The flow field is similar to that in Fig. 5 but with opposite directions.

Fig. 8 shows a comparison of the $\overline{V}$ velocity distribution at the middle of region IV ($\overline{Y} = 0$) at different times subject to the nonslip and the slip boundary conditions. The velocity distributions at $\tau = 0$ are identical to those at $\tau = \pi$ but with opposite directions. The slip effect can also be clearly seen from the comparison. Fig. 9 compares the $\overline{V}$ velocity distributions at several different $\overline{Y}$ planes in region IV at $\tau = 0$. The $\overline{V}$ velocity distributions in the central region of the vortex are almost identical, but they are clearly different from those at the edge. Fig. 10 compares the $\overline{V}$ velocity distributions at two different $\overline{Y}$ planes (at the center and near the right edge) in region IV at $\tau = 0$ subject to the nonslip and the slip boundary conditions. The slip effect is clearly demonstrated.

Damping affects amplitude as well as frequency in a microcomb structure. Damping is therefore an important design parameter. The damping ratio is related to the quality factor by $\varsigma = 1/2Q$. The quality factor of the model system is defined by $\frac{1}{Q_s} = \frac{1}{Q_I} + \frac{1}{Q_{II}} + \frac{1}{Q_{III}} + \frac{1}{Q_{IV}}$. The subscription s represents the model system. Subscriptions I–IV represent sections I–IV, respectively. Table 2 compares the quality factors calculated by the numerical simulations and the analytical solutions. The energy dissipated in regions II and III was calculated using

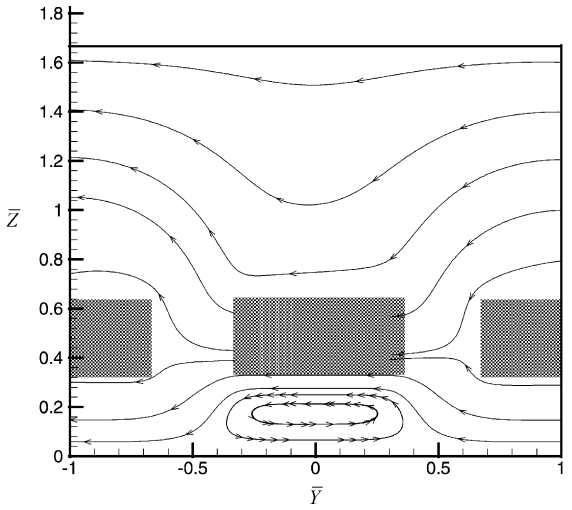

Fig. 7. The streamline plot at $\tau = \pi$ subject to the nonslip boundary conditions after the periodic steady state is reached.

$$D_{II} = 4 \int_{A_{II}} \int_{0}^{2\pi/4\omega} \Delta P v_0 \cos \omega t \, dt \, dA \tag{21}$$

where ΔP is the pressure difference between the right and left surfaces of the oscillating electrode. As demonstrated in the table, regions I and IV contribute 24% and 60% of the total damping, respectively. Regions II and III contribute about 16%.

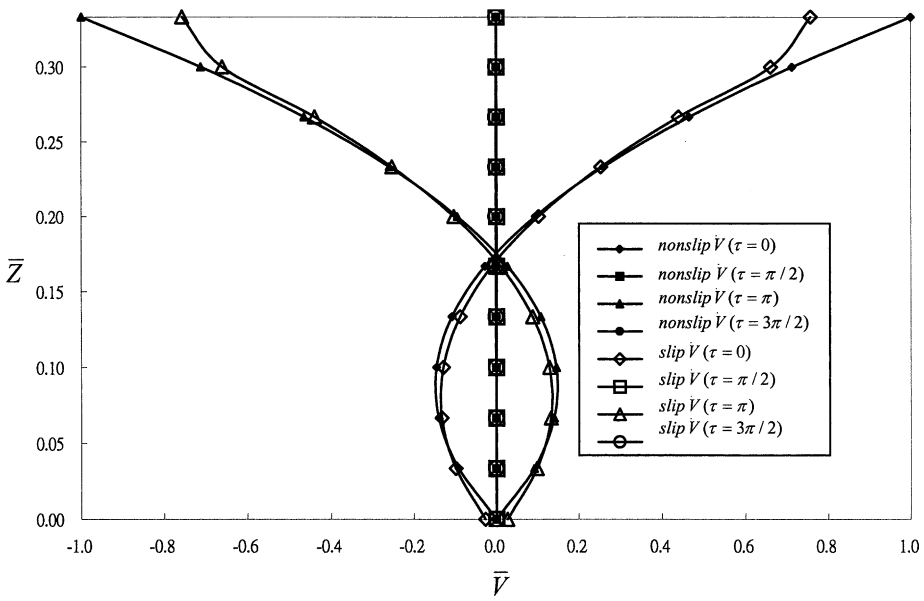

Fig. 8. The $\overline{V}$ velocity distributions along the $\overline{Z}$-coordinate at the center ($\overline{Y} = 0$) of region IV at different times after the periodic steady state is reached.

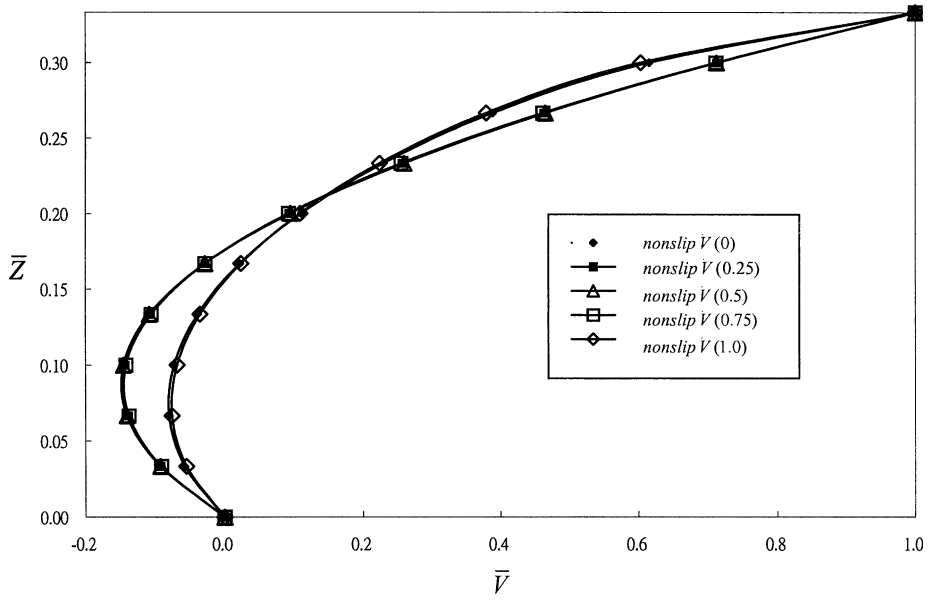

Fig. 9. The $\overline{V}$ velocity distributions in region IV along the $\overline{Z}$-coordinate at different $\overline{Y}$ locations, $\tau = 0$. The numbers 0, 0.25, 0.5, 0.75, and 1.0 on the legend denotes the left edge, a quarter width, a half width, three quarters width, and the right edge of the moving electrode, respectively.

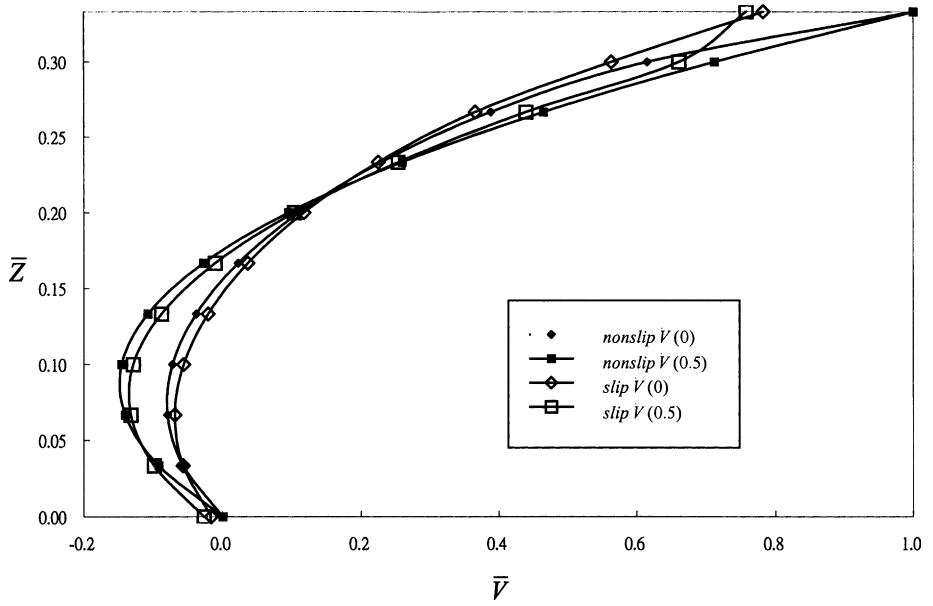

Fig. 10. The comparison of $\overline{V}$ velocity distributions in region IV along the $\overline{Z}$-coordinate at different $\overline{Y}$ locations subject to the nonslip and the slip boundary conditions, $\tau = 0$. The numbers 0 and 0.5 on the legend denotes the left edge and a half width of the moving electrode, respectively.

The numerical quality factor in region IV subject to the nonslip boundary conditions is larger than that subject to the slip boundary conditions by about 13%. This implies that the slip conditions give rise to less damping and therefore smaller viscous shear. The numerical quality factors in regions I and IV are both much smaller than that predicted by the analytical solutions (the Stokes flow model). The Stokes flow

Table 2
The comparison of analytical and numerical quality factors in different regions for the type I microcomb structure

	Region I	Region II and III	Region IV	The model system
Numerical quality factors subject to the nonslip boundary conditions	17.04	25.28	6.88	4.11
Numerical quality factors subject to the slip boundary conditions	16.52	26.59	7.78	4.41
Analytical quality factors (the Stokes flow model)	286.75	25.28	22.86	11.52

assumes that the oscillating electrode is an infinite plate in the $\overline{Y}$ direction. However, numerical simulations reveal that "the fluid brake effect" is quite significant in such flows. The fluid brake created by the pumping and sucking of the oscillating electrode decelerates the horizontal movement of the fluid. The velocity gradient between the fluid and the moving wall therefore becomes much larger than that predicted by the Stokes flow.

Although there is no experimental data on the type I microcomb structure to directly back up the conclusions of this study, the experimental data for type II microcomb structures conducted by Zhang and Tang [5] did suggest that the damping on the oscillating electrode was about 2–3 times higher than that predicted by the Stokes flow model. Even though numerical simulations on type II microstructures have not been reported, we guess that the explanations for Zhang and Tang's experimental results are probably similar to the conclusions in this study, because there are some similarities in configuration and movement between these two types of microstructures. Numerical simulations on type II microcomb structures are currently undertaken by the authors.

5. Conclusions

Previous investigators modeled the flow field of laterally oscillating microstructures as a Couette flow or Stokes flow. The numerical simulation results in this study demonstrate that the flow is much more complex and quite different from the Couette or Stokes flow. The major difference is caused by the fact that the pumping and sucking motions of the oscillating electrode creates a fluid brake effect. This fluid brake retards the horizontal movement of the fluid in regions I and IV. The fluid deceleration generates higher velocity gradients on the surfaces and gives rise to a greater damping. This fluid brake effect is quite strong, which increases the damping and therefore reduces the quality factor to about 36% of that predicted by the Stokes flow model. The flow in region IV consists of a strong vortex. This vortex flow depends strongly on the boundary conditions but very weakly on the $St\,Re$ and Re parameters. This is because the gap in region IV is much shorter than the penetration depth of the flow.

References

[1] T. Veijola, H. Kuisma, J. Lahdenpera, T. Ryhanen, Equivalent-circuit model of the squeezed gas film in a silicon accelerometer, Sens. Actuators A 48 (1995) 239–248.
[2] W.C. Tang, Electrostatic comb drive for resonant sensor and actuator applications, Ph.D. thesis, University of California, Berkeley, CA, 1990.
[3] W.C. Tang, T.C. Nguyen, M.W. Judy, R.T. Howe, Electrostatic-comb drive of lateral polysilicon resonators, Sens. Actuators A 21–23 (1990) 328–381.
[4] Y.H. Cho, B.M. Kwak, A.P. Pisano, R.T. Howe, Viscous energy dissipation in laterally oscillating planar microstructures: a theoretical and experimental study, in: Proceedings of IEEE Workshop on Microelectromechanical Systems, 1993, pp. 93–98.
[5] X. Zhang, W.C. Tang, Viscous air damping in laterally driven microresonators, in: Proceedings of IEEE Workshop on Microelectromechanical Systems, 1994, pp. 199–204.
[6] H.S. Carslaw, J.C. Jaeger, Conduction of Heat in Solids, Clarendon Press, Oxford, 1959, pp. 58–73.
[7] V.S. Arpaci, Conduction Heat Transfer, Addison-Wesley Publishing Co., Reading, MA, 1966, pp. 307–314.
[8] M.N. Ozisik, Heat Conduction, Wiley, New York, 1980, pp. 200–205.
[9] E.A. James, Gas Dynamics, second ed., Allyn and Bacon, Boston, 1933, pp. 316–329.
[10] K.A. Hoffman, S.T. Chiang, Computational Fluid Dynamics for Engineers—Volume I, Engineering Education System, Kansas, 1993, pp. 288–343.
[11] C.Y. Lee, L.J. Yang, P.H. Chen, The zeroth order solution of the velocity field around micro comb structures with lateral oscillation, J. Chin. Inst. Eng. 25 (1) (2002) 57–65.
[12] I.G. Currie, Fundamental Mechanics of Fluids, second ed., McGraw-Hill, Inc., New York, 1993, pp. 224–232.